International Shipbuilding Progress 60 (2013) 309–343
DOI 10.3233/ISP-130101
IOS Press

Confined water effects on the viscous flow around a tanker with propeller and rudder

L. Zou * and L. Larsson
Chalmers University of Technology, Gothenburg, Sweden

A ship travelling in canals or narrow channels may encounter hydrodynamic forces and moments caused by a nearby side bank. Since most canals are shallow the effect of the bottom can also be considerable. Knowledge of these effects is crucial for safe navigation. The present paper introduces a study in the framework of a project applying Computational Fluid Dynamics (CFD) in the prediction of confined water effects. Using a steady state Reynolds Averaged Navier–Stokes solver, this study investigates the shallow-water and bank effects on a tanker moving straight ahead at low speed in a canal characterized by surface piercing banks. The tanker is fitted with a rudder and a propeller at a zero propeller rate and at self-propulsion. In the systematic computations, a series of cases are considered with varying water depth and ship-to-bank distance, as well as different canal configurations. In the computations, the double model approximation is adopted to simulate the flat free surface. The non-rotating propeller is treated as an appendage composed of shaft and blades, while the operating propeller is approximated by body forces, simulated by a lifting line potential flow model. Validation of forces and moments against experimental data has been performed in previous studies. The emphasis of the present paper is placed on the effects on the flow field and the physical explanation of these effects.

Keywords: Confined water effects, computational fluid dynamics, hydrodynamic forces and moments, verification and validation, flow field analysis

1. Introduction

As long as a ship is surrounded by the water flow, the forces and moments acting on it are affected by the presence of solid boundaries of the flow field, such as a shallow seabed below the hull, or a side bank in the vicinity of the hull. The term "shallow-water effects" in this case refers to the influence from the seabed, and "bank effects" to the influence from the side bank. In a canal, often both effects are significant. The influence on flow and hydrodynamic quantities then results in significant changes in ship motion, and leads to problems in ship maneuvering and navigation. The explanation of confined water effects is that when the distance between the hull and the seabed or the side bank is narrowed, the flow is accelerated and the pressure is accordingly decreased, which induces a variation in the hydrodynamic characteristics. The produced hydrodynamic forces, especially in extremely shallow canals,

*Corresponding author. E-mail: zlu714@gmail.com.

may considerably affect the maneuvering performance of the ship, making it difficult to steer. The ship may collide with the side bank and/or run aground due to the so-called "squat" phenomenon. From this point of view, confined water effects are extremely important for ship navigation. In the past few decades, many investigations on confined water effects have been carried out, both experimentally and numerically. A notable event was the International Conference on Ship Maneuvering in Shallow and Confined Water: Bank Effects [13], at which the participants expressed broad concern about this problem and presented many interesting papers.

However, historical investigations of bank effects have mostly relied on experimental tools, such as model tests and empirical or semi-empirical formulae, which normally treat the bank effect as a function involving hull-bank distance, water depth, ship speed, hull form, bank geometry, propeller performance, etc. During the 1970s, Norrbin at SSPA, Sweden, carried out experimental research and then, based on the experiments, proposed empirical formulae to estimate the hydrodynamic forces for flooded [25], vertical [24] and sloping [24] banks. Li et al. [19] continued Norrbin's investigations and tested the bank effect in extreme conditions for three different hull forms (tanker, ferry and catamaran). The influence of ship speed, propeller loading and bank inclination was evaluated. Ch'ng et al. [3] conducted a series of model tests and developed an empirical formula to estimate the bank-induced sway force and yaw moment for a ship handling simulator. In recent years, comprehensive model tests in a towing tank have been carried out at Flanders Hydraulics Research (FHR), Belgium, to build up mathematical models for bank-effect investigations and to provide data for computation validation. Vantorre et al. [30] discussed the influence of water depth, lateral distance, forward speed and propulsion on the hydrodynamic forces and moments based on a systematic captive model test program for three ship models moving along a vertical surface-piercing bank. They also proposed empirical formulae for the prediction of ship-bank interaction forces. From extensive tests, Lataire et al. [15] developed a mathematical model for the estimation of the hydrodynamic forces, moments and motions taking into consideration ship speed, propulsion and ship/bank geometry.

Although empirical formulae are widely used for bank-effect predictions, they have their shortcomings due to the approximation. They should only be used for cases within a given range of hull forms and conditions. Otherwise, the prediction is barely reliable. To establish a mathematical model, a significant number of systematic and expensive model tests is always required. However, the most important weakness of most experiments and empirical relations is their inability to provide detailed information on the flow field, which can explain the flow mechanism behind the bank effects. In view of this, researchers resort to using numerical methods to deal with the phenomena of bank effects. Among existing numerical methods, the potential flow method is the most common one. For instance, the slender-body theory developed by Tuck [28,29] is still widely used for ship squat prediction in confined waters [10]. Other examples of the potential flow method are available in the studies by, e.g., Newman [23], Miao et al. [22] and Lee et al. [16]. All these references

only give quantitative predictions of the forces and moments on the hull travelling in canal or channel, but without any information on the flow field. Using a viscous flow method, Lo et al. [20] studied the bank effect on a container ship model using CFD software based on the Navier–Stokes equations. The effect of vessel speed and distance to bank on the magnitude and temporal variation of the yaw angle and sway force were reported. Some details of the predicted flow field are available in this work. Wang et al. [31] studied the vertical bank effects using a Reynolds Averaged Navier–Stokes (RANS) method. This study predicted viscous hydrodynamic forces on a Series 60 hull at varying water depth to draught ratios and ship-to-bank distances, as well as simulated the pressure distribution on the hull.

In an ongoing project at Chalmers a CFD method is used in the prediction of confined water effects, such as shallow-water effects, bank effects and the ship-to-ship interaction. Regarding the investigation of shallow-water and bank effects, validation of viscous forces and moments against experimental data has been presented in three reports: Zou et al. [34,35] and Zou [33]. In these reports, forces and moments predicted by a RANS solver have shown reasonable correspondence with the measurements in terms of the variation of water depth and ship-bank distance. To further extend the investigation of confined-water effects in [34], the present paper aims at explaining the effects on the flow field and the physical explanation of these effects.

2. Geometries and test conditions

The test cases for systematic computations were determined from straight-line captive model tests for a second variant of the KRISO Very Large Crude-oil Carrier (KVLCC2).

The KVLCC2 tanker is characterized by more U-shaped stern sections than the first variant, KVLCC1. In Fig. 1 the KVLCC2 is represented by solid lines. This hull has been used extensively for CFD validation studies in other areas. In the tests, the model hull had a scale ratio $1/75$, and its principal dimensions were: length between perpendiculars $L_{PP} = 4.267$ m, beam $B = 0.773$ m, draught $T = 0.277$ m. In addition, it was fitted with a horn-type rudder and with a propeller either at a zero propeller rate (revolutions per minute rpm $= 0$) or at self-propulsion (measured rpm $= 345$). More details of the rudder and propeller geometries are listed in Tables 1 and 2.

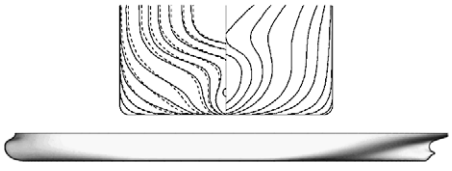

Fig. 1. KVLCC2 geometry.

Table 1
Rudder data (model scale)

Type	Horn
Section	NACA0018
Wetted surface area (m^2)	0.0486
Lateral area (m^2)	0.0243

Table 2
Propeller data (model scale)

Name	MOERI KP458
Type	Fixed pitch
No. of propeller	Single
No. of blades	4
Diameter D_R (m)	0.131
Pitch ratio $P_R/D_R(0.7R)$	0.721
Expanded area ratio A_E/A_0	0.431
Rotation	Right hand
Hub ratio	0.155
Skew (°)	21.150
Rake (°)	0.000

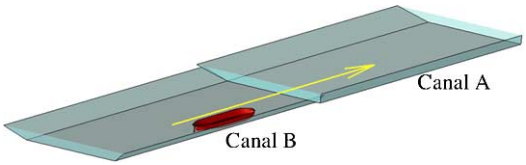

Fig. 2. Geometry of the towing tank built with two canals. (Colors are visible in the online version of the article; http://dx.doi.org/10.3233/ISP-130101.)

The captive model tests were made in two canals (A and B), built up in the shallow water towing tank at the Flanders Hydraulics Research (FHR) in co-operation with the Maritime Technology Division of Ghent University, Belgium. The KVLCC2 tanker was tested at a speed $U_0 = 0.356$ m/s (6 knots full scale) along one side of the canals, i.e. it moved close to the vertical bank (Canal A) and the bank with slope 1 : 1 (Canal B) at its starboard side. A brief illustration of the Canal A and Canal B configurations shaped by surface-piercing banks is given in Fig. 2 (the arrow indicates the direction of motion), and cross-section profiles of the two canals are further presented in Fig. 3. The tests in Canal A and Canal B were conducted at three different under keel clearances (*UKC*), namely 50%, 35% and 10% of the draught (water depth to ship draught ratio $h/T = 1.50, 1.35, 1.10$), and at four different lateral positions (ship-bank distance) chosen in combination with the water depth [34]. The

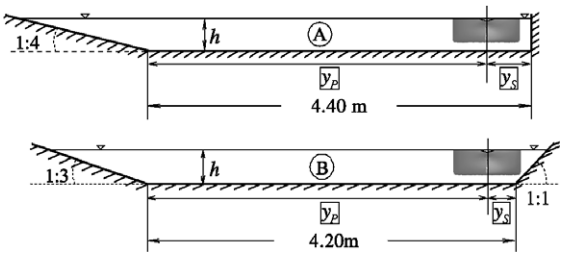

Fig. 3. Cross-sections of Canal A (*top*) and Canal B (*bottom*), seen in the direction of motion.

Table 3
Matrix of test conditions

y_B	Canal A			
	1.180	1.316	1.961	2.431
	Canal B			
h/T	0.758	0.909	1.632	2.173
1.50 ($UKC = 50\%T$)		0		
1.35 ($UKC = 35\%T$)	0/345	0/345	0/345	0/345
1.10 ($UKC = 10\%T$)		0		

non-dimensional ship-bank distance y_B is defined as below, following the proposals by e.g., Ch'ng et al. [3]:

$$\frac{1}{y_B} = \frac{B}{2}\left(\frac{1}{y_P} + \frac{1}{y_S}\right), \tag{1}$$

y_P, y_S represents the respective distance from the ship center-plane to the toe of the bank at the port/starboard side. This description thus takes two side banks into consideration, due to the non-uniform bank geometries and canal configurations.

A subset of the test conditions was selected for the validation including variations of the water depth and the ship-bank distance. Details are shown in Table 3. "0" represent the test cases with only a non-rotating propeller (rpm $=$ 0), while "0/345" indicate cases with the propeller both at a zero rpm and at self-propulsion (rpm $=$ 345). As can be seen, there are six water depth and ship-bank distance combinations in each canal, some of which rather extreme, which put the computational tools to a severe test. No waves are considered, since the tanker moves at a low speed ($U_0 = 0.356$ m/s). The corresponding Froude number is $Fr = U_0/\sqrt{gL_{PP}} = 0.055$ (largest depth Froude number $Frh = U_0/\sqrt{gh} = 0.206$) and the Reynolds number is $Re = U_0 \cdot L_{PP}/\nu = 1.513 \times 10^6$ (g is the acceleration of gravity and ν is the kinematic viscosity of water). As a result, the double model approximation is adopted and no sinkage and trim is considered.

3. Computational method

In CFD, the fluid motion around a hull is governed by a system of equations consisting of the Navier–Stokes equations (2) and the continuity Eq. (3), describing the conservation of momentum and of mass. Assuming the viscous flow around the KVLCC2 tanker to be incompressible, the governing equations given in a Cartesian coordinate system read [14]:

$$\frac{\partial u_i}{\partial t} + \frac{\partial}{\partial x_j}(u_j u_i) = -\frac{1}{\rho}\frac{\partial p_e}{\partial x_i} + F_i + \nu \frac{\partial^2 u_i}{\partial x_j \, \partial x_j}, \tag{2}$$

$$\frac{\partial u_i}{\partial x_i} = 0, \tag{3}$$

where $u_{i(j)}$ represents velocity components, $x_{i(j)}$ denotes coordinates, p_e is the pressure, v is the kinematic viscosity, F_i represents the body force (such as gravity) and ρ is the fluid density. For a three dimensional flow, i, $j = 1, 2, 3$. As four variables $(u_{i(j)}, p_e)$ are present in Eq. (2), the Navier–Stokes equations combined with the continuity equation, establish a closure of the equations system. To solve the governing equations, several methods are available, depending on the degree of approximation or modeling for the turbulent flow. In the present study the RANS method is adopted, since it is at present the best approximation considering both accuracy and the computing expense. The RANS method in theory simulates only the mean fluid motion by averaging the Navier–Stokes equations over time. Thus, time averaging Eqs (2) and (3) gives:

$$\frac{\partial \bar{u}_i}{\partial t} + \frac{\partial}{\partial x_j}(\bar{u}_j \bar{u}_i) = -\frac{1}{\rho}\frac{\partial \bar{p}_e}{\partial x_i} + F_i + \frac{1}{\rho}\frac{\partial}{\partial x_j}(\bar{\sigma}_{ji} + R_{ji}), \tag{4}$$

$$\frac{\partial \bar{u}_i}{\partial x_i} = 0, \tag{5}$$

$\bar{u}_{i(j)}$, $\bar{p}_e$ and $\bar{\sigma}_{ij}$ denote the average velocity, pressure and stress. $R_{ji} = R_{ij} = -\rho\overline{u_i' u_j'}$ is termed "Reynolds stresses" and is a symmetric quantity. As seen in Eqs (4) and (5), the fluctuating values are all removed during the time-averaging, but new unknown variables, the Reynolds stresses R_{ji}, are introduced. R_{ji} needs to be modeled to close the system of Eqs (4) and (5), which then yield all the mean flow properties. This procedure is known as turbulence modeling.

4. CFD solver

A steady state CFD solver for ship hydrodynamics, SHIPFLOW [2], was utilized for the numerical computations in the present work. It contains a RANS solver,

XCHAP, based on the finite volume method. In XCHAP, the discretization of convective terms is implemented by a Roe scheme [27] and for the diffusive fluxes central differences are applied. To approach second order accuracy, a flux correction is adopted [6]. An Alternating Direction Implicit scheme (ADI) is utilized to solve the discrete equations. Two turbulence models are available in XCHAP: the Shear Stress Transport k–ω model (k–ω SST model) [21] and the Explicit Algebraic Stress Model (EASM) [5,9]. As for the specified boundary conditions, the available options are: inflow, outflow, no-slip, slip and interior conditions. (a) Inflow condition: is normally satisfied at an inlet plane of the computational domain to guarantee an undisturbed flow in front of a hull. In XCHAP it specifies a fixed velocity equal to the ship speed and estimated values of k and ω. The pressure gradient normal to the inlet plane is set to zero. (b) Outflow condition: describes zero normal gradients of velocity, k, ω and fixed pressure at a downstream outlet plane of the domain far behind a hull. (c) No-slip condition: simulates a solid wall boundary (e.g. a hull surface) by designating zero value to velocity components, k, normal pressure gradient, and treating ω following [12]. (d) Slip condition: specifies the normal velocity component and normal gradient of all other flow quantities (e.g. pressure) as zero. It simulates a symmetry condition on flat boundaries. (e) Interior condition: describes the boundary data by interpolation from another grid.

5. Computational setup

Due to the asymmetry of the bank geometry and so the flow field, the computational domain has to cover the flow field around the whole hull in the canal. A schematic diagram indicating the coordinate system and the computational domain for Canal A and Canal B is given in Fig. 4. As presented in the figure, the coordinate system is defined as a body-fixed and right-handed Cartesian system, with the origin at the intersection of the flat free surface, the ship center-plane and the mid-ship section. The axes x, y, z are directed towards the bow, to starboard and downwards, respectively.

The computational domain is made up by seven boundaries: inlet plane, outlet plane, hull surface, flat free surface, seabed boundary, as well as two side banks. The inlet plane is located at $1.0L_{PP}$ in front of the fore-perpendicular (F.P.) and the outlet plane is at $1.5L_{PP}$ behind the aft-perpendicular (A.P.). The flat free surface is considered at $z = 0$, while the seabed and the two side banks are placed at specific locations as seen in Table 3. As to the adopted boundary conditions in the computations, the no-slip condition is satisfied on the hull surface (no wall function is introduced and the non-dimensional wall distance $y^+ < 1.0$ is employed instead); the inflow/outflow condition is set at the respective inlet/outlet boundary plane; the slip condition is set at the flat free surface ($z = 0$), the seabed and the side banks.

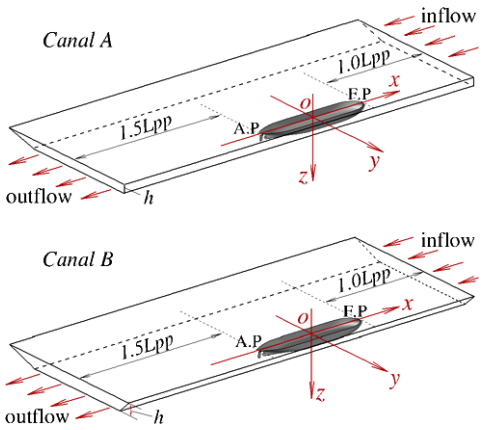

Fig. 4. Computational domain and coordinate system of Canal A and Canal B. (Colors are visible in the online version of the article; http://dx.doi.org/10.3233/ISP-130101.)

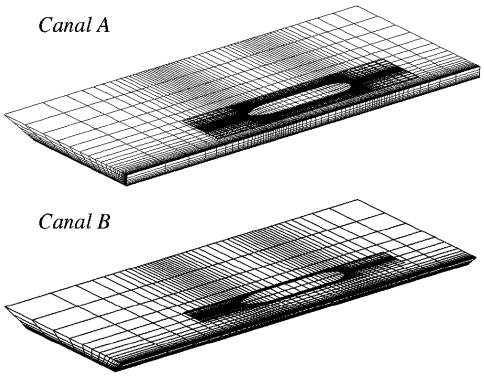

Fig. 5. Sketch of grid distribution in Canal A and Canal B.

6. Grid generation

For resolving the complex flow field in the present study, it is impossible to create a grid with only one block around all the geometries (hull, appendage(s) and shallow canals). To ensure an appropriate grid quality, the overlapping grid technique available in SHIPFLOW was applied in the computations. As illustrated by an example with coarse grid distributions in Fig. 5 for Canal A and Canal B (excluding the propeller), the overlapping grid is mainly built up by three components: a cylindrical H–O grid for hull geometry, a curvilinear O–O grid defining the rudder geometry and a rectilinear H–H grid specifying the canal geometry.

The H–O and O–O grids are immersed in the H–H grid. The body-fitted H–O grid is produced to cover the main flow field around the hull, in which two clusters of

grid points are concentrated around the bow and stern regions so as to resolve the flow field more precisely. A small outer radius ($0.2L_{PP}$) of the cylindrical grid is used for Canal A to save grid points and an even smaller radius ($0.12L_{PP}$) of the cylindrical H–O grid is applied for Canal B. The body-fitted component O–O type grid is generated internally to describe the rudder. Finally, a "box" of the rectilinear H–H grid is employed to take care of the remaining part of the domain within the inflow plane, outflow plane, seabed and side banks.

7. Experiences from a previous verification and validation study and an investigation of modeling error

Prior to the systematic computations, a preliminary verification and validation (V&V) study was performed [33] to assess the numerical error and to clarify the modeling error in the computations. This was accomplished through a grid convergence and formal validation study for the predicted forces and moments. In this section, a brief description of the study and the results are introduced.

For the grid convergence study a representative test was set up, with its basic specification comparable with that of the systematic computations. A KVLCC2 model tanker (scale factor $1/45.714$) moved slowly at $U_0 = 0.530$ m/s ($Fr = 0.064/Frh = 0.237$, $Re = 3.697 \times 10^6$) in a shallow canal with vertical, surface piercing side banks. No appendage was attached to the tanker, but the condition was quite extreme: $h/T = 1.12$ and a non-dimensional ship-to-bank distance $y_B = 0.6B$. The canal configuration is given in Fig. 6, indicating that the hull is moving close to the bank on the port side of the canal. Computational settings (coordinates system, domain, grid generation, boundary conditions, etc.) in the grid convergence study were in accordance with the descriptions in the previous sections.

The estimation of numerical errors and uncertainties followed the proposal by Eça et al. [7,8], see the Appendix. Six systematically refined grids were created with a uniform grid refinement ratio $r = \sqrt[4]{2}$ to enable a curve fit by the Least Squares Root method, so as to minimize the impact of scatter on the determination of grid convergence. The grid convergence study was made for the non-dimensional longitudinal force (X'), sway force (Y'), roll moment (K') and yaw moment (N'), which are defined as follows:

$$X' = X/\left(0.5\rho U_0^2 L_{PP} T\right), \qquad Y' = Y/\left(0.5\rho U_0^2 L_{PP} T\right),$$
$$K' = K/\left(0.5\rho U_0^2 L_{PP} T^2\right), \qquad N' = N/\left(0.5\rho U_0^2 L_{PP}^2 T\right).$$

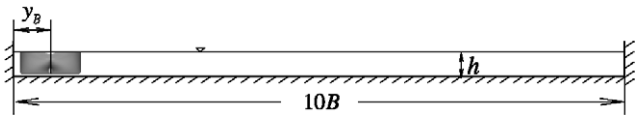

Fig. 6. Canal configuration in grid convergence study.

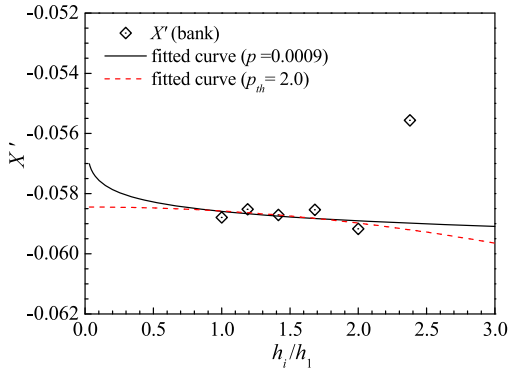

Fig. 7. Grid convergence of X'. (Colors are visible in the online version of the article; http://dx.doi.org/10.3233/ISP-130101.)

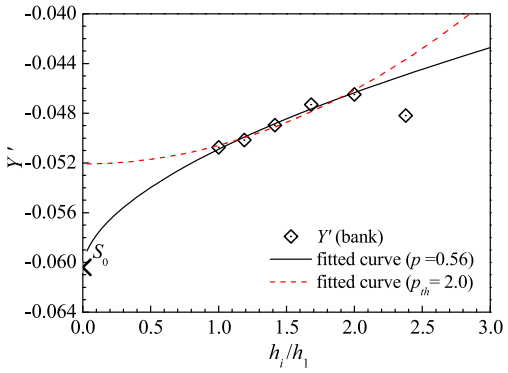

Fig. 8. Grid convergence of Y'. (Colors are visible in the online version of the article; http://dx.doi.org/10.3233/ISP-130101.)

Their grid convergence plots (including fitted curves both from an estimated order of accuracy p and from a theoretical order of accuracy $p_{th} = 2.0$) are presented in Figs 7–10, and the estimated numerical uncertainties U_{SN} (for finest Grid 1 to medium Grid 3) are shown in Table 4, where S represents the numerical solution for each grid. Note that the coarsest Grid 6 is dropped from the curve fit since it contaminates the results. As seen in the grid convergence figures, the X' and K' solutions apparently oscillate around the fitted curves (oscillatory convergence), and are almost independent of the grid density, producing fitted curves as nearly horizontal lines. Y' solutions present a slightly better convergence trend, but still very slow. The most satisfactory grid convergence appears in the N' solutions, as the points are all on the fitted curve, and most importantly, the estimated order of accuracy is identical to the theoretical one, $p = p_{th} = 2.0$. As for the estimated U_{SN}, an oscillatory convergence in X' and K' is noted again since the value fluctuates slightly between

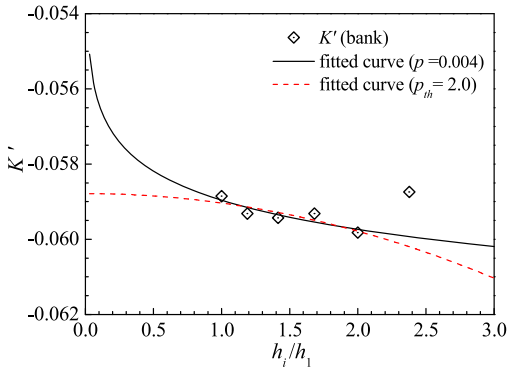

Fig. 9. Grid convergence of K'. (Colors are visible in the online version of the article; http://dx.doi.org/10.3233/ISP-130101.)

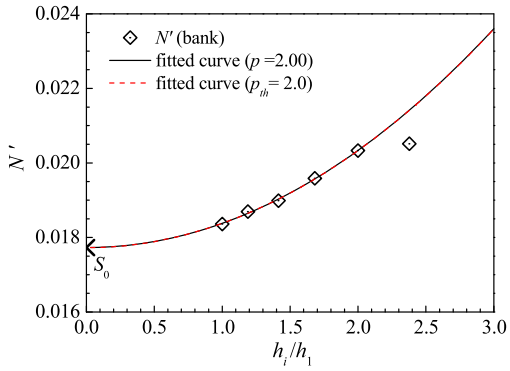

Fig. 10. Grid convergence of N'. (Colors are visible in the online version of the article; http://dx.doi.org/10.3233/ISP-130101.)

Table 4
Numerical uncertainties of X', Y' and K', N'

	X'	Y'	K'	N'
p	0.0009	0.56	0.004	2.00
$\|U_{SN}\%S\|_1$	3.32	24.45	4.95	4.54
$\|U_{SN}\%S\|_2$	3.34	26.21	4.91	6.67
$\|U_{SN}\%S\|_3$	3.33	29.91	4.90	8.54

Grid 1, Grid 2 and Grid 3. Uncertainties in Y' and N' tend to be converged. However, Y' presents a slower convergence and its numerical uncertainty is much larger.

From the grid convergence study, it seems very difficult to obtain grid convergence in bank-effects computations, even with a fine grid discretization (i.e. approximately,

8 million grid points). Considering both the accuracy and the computing expense, a density similar to that of Grid 3 was adopted in the systematic computations.

At the first stage of systematic investigations, the computations were made for the tests with only non-rotating propeller in Canal A. The EASM model was applied and to simplify the computation, the still propeller was not included. The measured total resistance with deducted thrust was used for direct comparison with the predicted resistance (namely X'). Following a procedure in the ASME V&V 20 2009 standard [1], a formal validation study was performed for the test condition $h/T = 1.1$ and $y_B = 1.316$ in Canal A, in combination with the experimental data from FHR.

In the procedure, the concepts of a validation uncertainty $U_{val}(U_{val}^2 \approx U_{num}^2 + U_D^2)$ and a comparison error $|E| = |S - D|$ are introduced. S is the numerical solution and U_{num} is its uncertainty. D and U_D represent the experimental data and the corresponding uncertainty. Comparing U_{val} and $|E|$, if $|E| \leqslant U_{val}$, the modeling error is within the "noise level" imposed by the numerical and experimental uncertainty, and not much can be concluded about the source of the error; but if $|E| \gg U_{val}$, the sign and magnitude of E could be used as to improve the modeling. In the validation study, the numerical uncertainty U_{num} was approximated as the grid discretization uncertainty U_{SN} estimated from the grid convergence study (the iterative uncertainty was neglected), while the data uncertainty U_D was available from FHR [4]. The estimated uncertainties and comparison errors for hydrodynamics quantities X', Y', K', N' are presented in Table 5, where the measured data (D) are used for normalization. As can be seen from the validation study, Y' and N' present a larger comparison error than validation uncertainty, implying that there were significant modeling errors in computations and/or measurements.

An investigation of modeling errors in the computations was then carried out by evaluating the influence of neglected waves, non-free sinkage and trim, turbulence modeling and absence of propeller. The investigation indicated that the wave effect was negligible, and the influence of sinkage and trim was generally very small, however, it could not be neglected for the K' and N' moments at the very shallow water depth ($h/T = 1.1$). As for the turbulence model, the Menter k–ω SST model was applied for the same computations and it produced slightly better results than the EASM model. Furthermore, including the non-rotating propeller was shown to be important, especially for the longitudinal force X'.

According to the investigation of modeling errors, the computations should be improved to increase the accuracy taking the sources of modeling error into consideration. Therefore based on their significance in specific conditions: the Menter

Table 5
Validation results of X', Y', K', N'

	X'	Y'	K'	N'
$\|U_D\%D\|$	4.40	18.80	7.10	2.78
$\|U_{SN}\%D\|$	3.27	8.38	3.57	6.92
$\|U_{val}\%D\|$	5.48	20.58	7.95	7.46
$\|E\%D\|$	1.85	71.99	27.19	18.94

k–ω SST model was used for turbulence modeling, the computed initial sinkage and trim were added for the tests at the shallowest water depth ($h/T = 1.1$), while the propeller geometry was included in the test conditions with rpm $= 0$. Finally, the computations were extended to all the test conditions for Canal A and Canal B (in Table 3), including the rotating propeller with varying ship-bank distance. It should be noted that some of the modeling improvements have been presented before [33,34], but the present paper is the first where all improvements have been introduced in a systematic way. Also, the rotating propeller is introduced here for the first time.

8. Propeller simulation

For predicting propeller performance, the non-rotating propeller (zero rpm) was simply treated as a fixed appendage composed of propeller shaft and four blades. In SHIPFLOW, the rotating propeller is approximated by body forces in the propeller disc, specified as a cylindrical component grid embedded into the hull grid. The forces, transferred to XCHAP, are obtained from a lifting line potential flow model with an infinite number of blades. Therefore, the force at each point in the propeller disc is independent of time, approximating a propeller-induced steady flow. The lifting line model is interactively coupled with the XCHAP at every ten iteration steps, and the effective wake field and the forces are consequently produced. Thus, the fluid flow passing through the volume grid cells at the propeller disc is accelerated and the propeller behavior is simulated. More comprehensive specifications of this lifting line model are given in [18,32], and some early applications of this model are available in [11,32].

The main computational settings have been introduced in previous sections. However, the propeller grids were not discussed. Examples of the hull-propeller-rudder surface meshes are presented in Fig. 11(a) and (b) with coarse densities for clarity. Note the difference in grids for the non-rotating and rotating propellers.

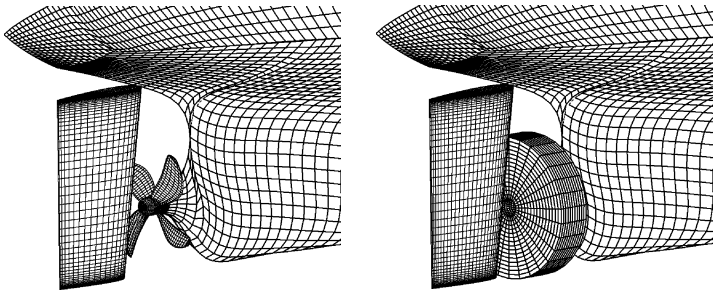

(a) (b)

Fig. 11. Surface meshes of hull, propeller and rudder. (a) With non-rotating propeller. (b) With rotating propeller (body force).

9. Forces and moments

In this section, hydrodynamic forces X', Y' and moments K', N' from varying water depths and ship-bank distances in Canal A and Canal B are presented. The predicted flow field will be shown in the following sections. All the computed forces and moments are compared with the test data from FHR. It should be noticed that the measured data were obtained in a confidential project, so that the absolute values of the data and computed results are hidden in the following figures, and only zero values are given for reference. Results from the variation of water depth are shown in Figs 12 and 13 for Canal A and B respectively. As for the varying ship-bank distance at $h/T = 1.35$, results with the non-rotating (0-rpm) and rotating propeller (self) are presented in Fig. 14 for Canal A and in Fig. 15 for Canal B.

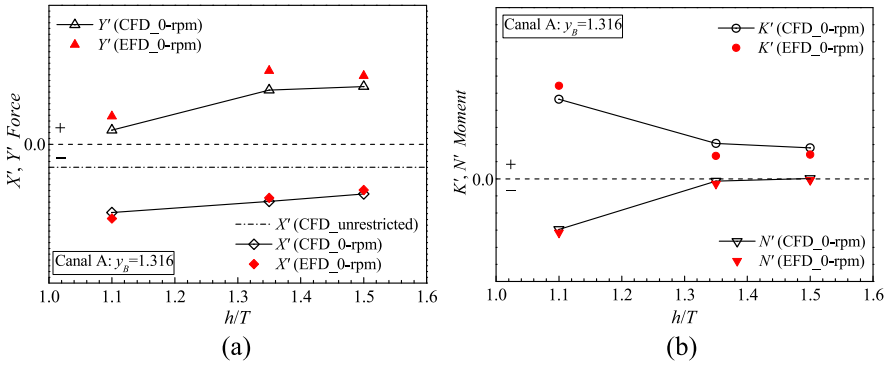

Fig. 12. X', Y' force and K', N' moment versus h/T in Canal A. (a) X', Y' force. (b) K', N' moment. (Colors are visible in the online version of the article; http://dx.doi.org/10.3233/ISP-130101.)

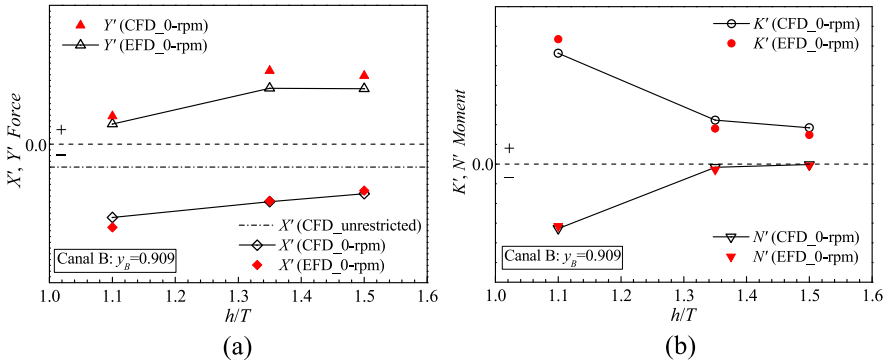

Fig. 13. X', Y' force and K', N' moment versus h/T in Canal B. (a) X', Y' force. (b) K', N' moment. (Colors are visible in the online version of the article; http://dx.doi.org/10.3233/ISP-130101.)

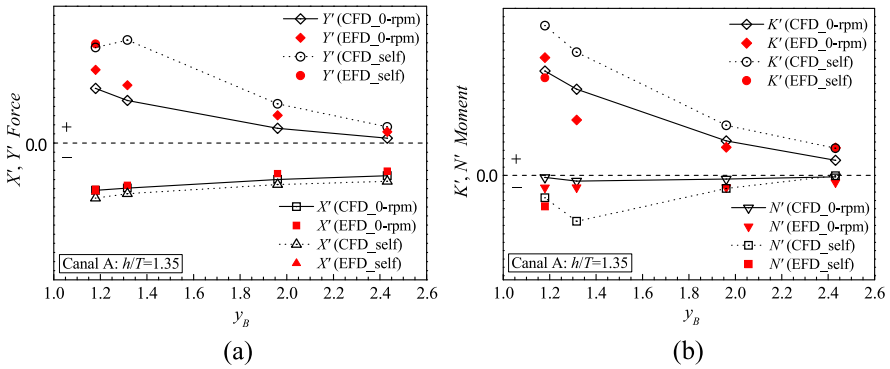

Fig. 14. X', Y' force and K', N' moment versus y_B in Canal A. (a) X', Y' force. (b) K', N' moment. (Colors are visible in the online version of the article; http://dx.doi.org/10.3233/ISP-130101.)

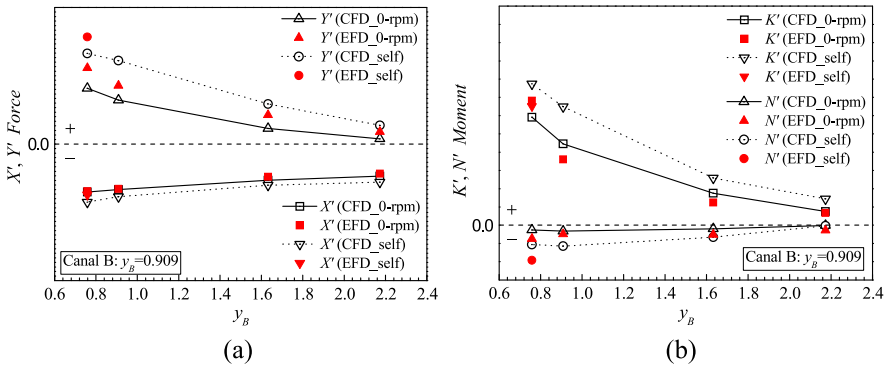

Fig. 15. X', Y' force and K', N' moment versus y_B in Canal B. (a) X', Y' force. (b) K', N' moment. (Colors are visible in the online version of the article; http://dx.doi.org/10.3233/ISP-130101.)

Compared with measurements, the tendencies of hydrodynamic forces and moments are captured well in both canals. As seen in Figs 12 and 13, the X' force and K' moment increase when the hull bottom approaches the seabed, while the Y' force (a suction force towards the bank) behaves in a different way. It is almost unchanged between $h/T = 1.5$ and 1.35, but drops rapidly between $h/T = 1.35$ and 1.1. The N' moment shows a monotonic increase for diminishing water depth, but is very small for the larger depths. The tendencies are very similar for both canals.

Results for varying bank distance at the same water depth $h/T = 1.35$ are presented in Figs 14 and 15. The cases with non-rotating propeller exhibit good correspondence between computed X' results and measured data and the trends are well predicted for the Y' force and K' and N' moments. It is seen that both forces, X' and Y', increase monotonically when the bank is approached, as does the heeling

moment K'. The N' moment is almost constant and very small over the whole range of distances. Again, the trends are very similar in both canals.

For the rotating propeller, the only available data is for the closest distance. There is generally a good prediction of the change of the variables at this distance due to the propeller. This holds for X', Y' and N' and for both canals. However, the change in K' has the wrong sign. All predicted forces and moments exhibit an increase due to the propeller. In particular, the N' moment changes from very small to significant.

10. Pressure distributions

To facilitate the understanding of predicted viscous forces and moments and of the mechanism of confined-water effects, this section presents the predicted pressure distributions on the hull (C_P, normalizing the pressure by $0.5\rho U^2$), which have a direct connection with the resulting forces and moments. In particular, the pressure difference between the two sides of the hull is shown below each pressure distribution. The purpose is to ensure a straightforward impression of its contribution to the forces and moments, among which contributions to the lateral force Y' and yaw moment N' are of most interest. Considering the fact that the starboard side of the hull always faces the close side bank and encounters the largest influence from this bank, the pressure difference $\Delta C_{P(S-P)}$ is presented on the starboard side and its value is obtained by subtracting the pressure on the port side from that on the starboard side $(S - P)$. It should be mentioned that no measured flow field is available, therefore in this and following sections, only computed flow field will be presented.

In Fig. 16(a)–(c), C_P and $\Delta C_{P(S-P)}$ for varying water depth with non-rotating propeller in Canal A are presented, while results in Canal B are shown in Fig. 17(a)–(c). Solid contour lines represent positive pressure, while dashed contour lines indicate negative values. A clear difference in the pressure distribution between the water depths at this specific ship-bank distance is shown in these figures. The larger the clearance between the hull and the seabed, the smaller the pressure variations along the hull.

In general, a high pressure region is noted at the bow due to stagnation, and its size and value are largest at the shallowest water depth $h/T = 1.1$. At this depth there is also a large region of low pressure that covers the parallel middle body of the hull in both canals, resulting from the blockage effect. Since in these cases the ship-bank distance is also small ($y_B = 1.316$ in Canal A, $y_B = 0.909$ in Canal B), the blockage comes from both the bank and the shallow water. But the shallow-water effect is slightly stronger, as the largest reduction happens on the bottom of the fore-body, and in Canal B this reduction region is larger because the space between the hull and seabed/bank is smaller due to the sloping bank, see Figs 16(a) and 17(a).

On the fore-body the flow entering into the narrow gap between the hull and the seabed/bank is accelerated, giving rise to the decrease of the pressure. However the low pressure is not maintained over the whole hull. Instead, the pressure increases (but still with negative values) on the aft-body. The explanation is that the high-speed

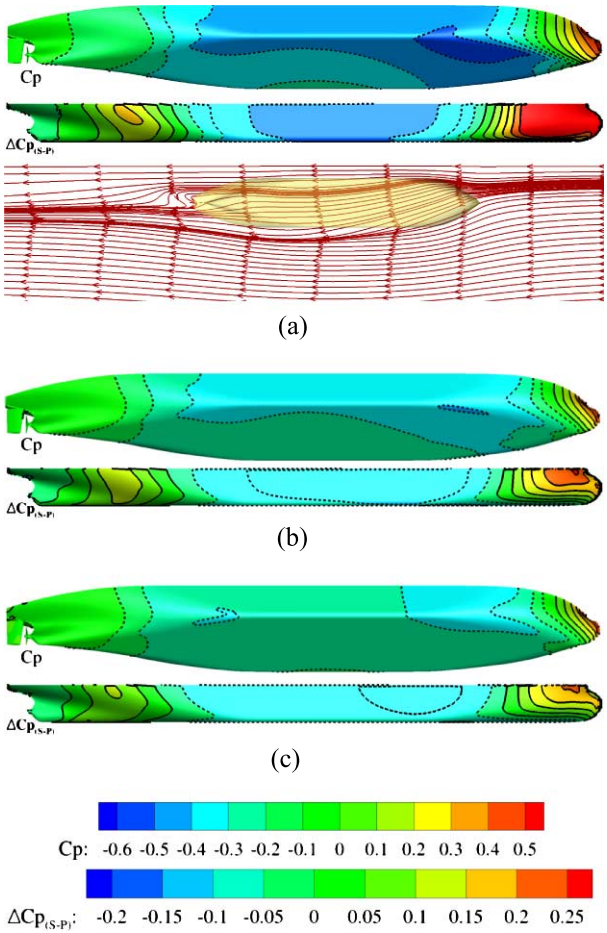

Fig. 16. Pressure distribution and difference against h/T ($y_B = 1.316$) in Canal A with *non-rotating* propeller. (a) C_P, $\Delta C_{P(S-P)}$ and streamlines on the seabed at $h/T = 1.1$. (b) C_P and $\Delta C_{P(S-P)}$ at $h/T = 1.35$. (c) C_P and $\Delta C_{P(S-P)}$ at $h/T = 1.5$. (Colors are visible in the online version of the article; http://dx.doi.org/10.3233/ISP-130101.)

flow from the bow is slowed down. Some of the flow escapes towards the port side. This is clearly seen from the streamlines over the seabed in Canal A, seen from the bottom of the seabed in Fig. 16(a). A remarkable cross flow towards the port side is developed under the fore-body, so the flow speed at the stern is reduced comparing with that at the fore-body. The notable flow separation at the stern at the shallowest water depth also gives rise to a large pressure difference between the bow and stern, thus a large resistance (X' force) is expected. This will be discussed in a separate section below.

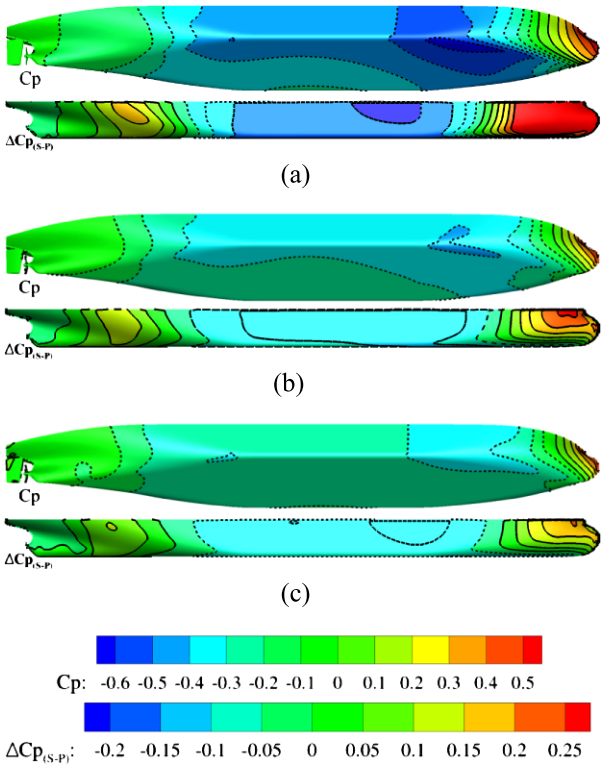

Fig. 17. Pressure distribution and difference against h/T ($y_B = 0.909$) in Canal B with *non-rotating* propeller. (a) C_P and $\Delta C_{P(S-P)}$ at $h/T = 1.1$. (b) C_P and $\Delta C_{P(S-P)}$ at $h/T = 1.35$. (c) C_P and $\Delta C_{P(S-P)}$ at $h/T = 1.5$. (Colors are visible in the online version of the article; http://dx.doi.org/10.3233/ISP-130101.)

Turning next to the pressure difference between starboard and port sides for understanding the trends of the forces and moments in Figs 12 and 13, a decrease of the pressure difference is noted with an increasing clearance between the hull and the seabed. At all water depths, however, a positive difference is presented at the bow and stern, while negative difference is shown on the parallel middle body. The former generates a force pushing the hull away from the side bank, and the latter is an attraction force towards the bank. At $h/T = 1.1$, the region with negative pressure difference covers the whole parallel middle body and generates a large force towards the bank. However the positive pressure differences at the bow has a large magnitude and produces a large repulsion force which more or less balances with the attraction. Therefore, the Y' force is relatively small at the smallest water depth. With an increase of water depth, the positive pressure at the bow is dramatically reduced and the pressure at the stern contributes very little, so the negative pressure dominates and a larger attraction force (Y') is produced. While the whole hull is attracted to-

wards the bank, a bow-out yaw moment N' is produced as the positive pressure at the bow is much larger than that at the stern. N' is reduced with increasing water depth due to the decrease of the pressure difference at the bow. Thus, using the pressure distributions, the tendencies of forces and moments against water depth can be explained.

As for C_P and $\Delta C_{P(S-P)}$ in the variation of ship-bank distance, cases with non-rotating and rotating propellers are presented for parallel comparisons. Results with non-rotating propeller in Canal A are shown in Fig. 18(a)–(d) and with rotating propeller in Fig. 19(a)–(d). For Canal B the corresponding results are presented in Fig. 20(a)–(d) and Fig. 21(a)–(d).

With non-rotating propeller at a small ship-bank distance, significant pressure reductions are again noticed at the starboard side and at the bottom, see Figs 18 and 20.

When the hull moves far away from the bank, the low pressure regions are reduced, exhibiting a combined bank and shallow-water effects. This is in accordance with the observation in the variation of the water depth. As to the pressure difference, at the closest distance ($y_B = 1.180$ in Canal A, $y_B = 0.758$ in Canal B) a high positive difference is observed at the bow but the area is much smaller than that of the negative difference on the middle body. Therefore the lateral force Y' is dominated by the negative difference and draws the hull towards the bank. With increasing y_B, the positive and negative pressures drop and tend to be comparable, leading to a decreasing Y' force, see Figs 14(a) and 15(a). At the largest distance, the negative difference disappears and the positive pressure also tends to zero. Thus almost no pressure difference is produced at that large distance and Y' is close to zero. The situation is similar for the yaw moment N' at large distances, but unlike the situation with a small water depth, N' does not attain a large value for small bank distances. The reason is that the high positive pressure difference region at the bow is smaller and that the negative difference at the shoulder is located more forwards in this case.

The pressure on the aft-body is different when the propeller is operating behind the hull. As seen in Figs 19 and 21, the pressure is decreased around the stern compared with that with a non-rotating propeller, and a new low pressure region appears at the shoulder of the aft-body. Just upstream of the propeller the reduction in pressure can be explained by the suction of the propeller. However, the additional pressure reduction at the aft-shoulder seems to have no direct correlation with the propeller. To look into this, the streamlines on the seabed are selected again. Taking the closest y_B in Canal A for instance, streamlines on the seabed (seen from the bottom) are shown in Fig. 18(a) with non-rotating propeller and in Fig. 19(a) with rotating propeller. When the propeller is not operating, the flow directed to port under the bow, continues to move in this direction, particularly aft of the hull. The flow is thus expanded sideward (the streamlines are more spread out) and the speed reduced due to continuity.

Note that the streamline inflexion in Fig. 18(a) is less pronounced in comparison with those in Fig. 16(a), as the water depth here is a medium one $h/T = 1.35$ and lower blockage of the flow is expected. A different streamline picture is illustrated

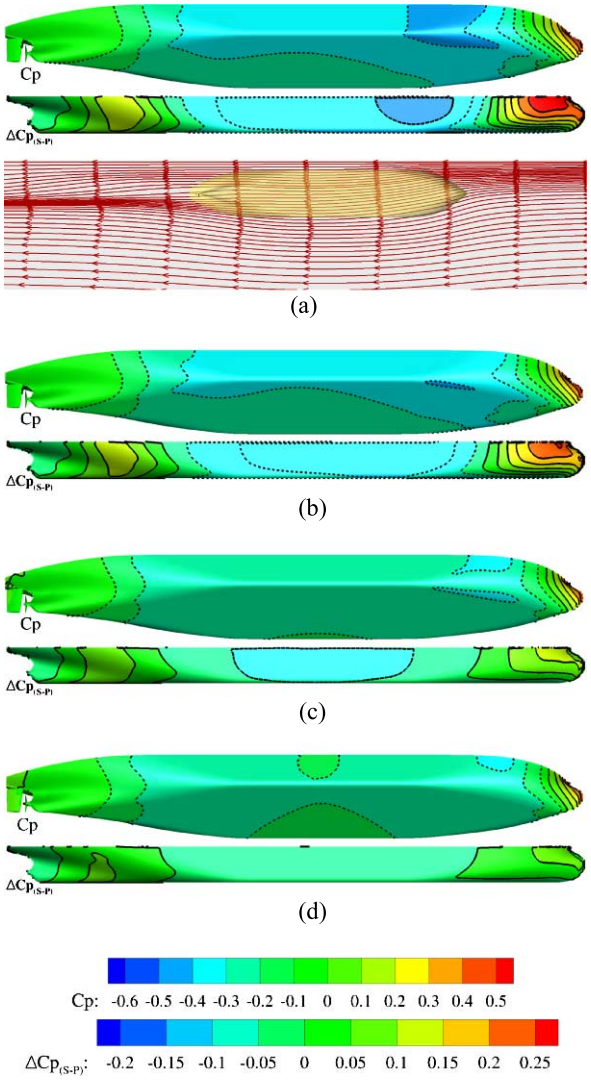

Fig. 18. Pressure distribution and difference against y_B ($h/T = 1.35$) in Canal A with *non-rotating* propeller. (a) C_P, $\Delta C_{P(S-P)}$ and streamlines at $y_B = 1.180$. (b) C_P and $\Delta C_{P(S-P)}$ at $y_B = 1.316$. (c) C_P and $\Delta C_{P(S-P)}$ at $y_B = 1.961$. (d) C_P and $\Delta C_{P(S-P)}$ at $y_B = 2.431$. (Colors are visible in the online version of the article; http://dx.doi.org/10.3233/ISP-130101.)

in Fig. 19(a) with a rotating propeller. Passing over the bow, a similar cross flow is generated towards the port side. However after the mid-ship, the flow turns back towards the starboard side due to suction of the operating propeller. Near the stern the flow moves to starboard, rather than to port. There is thus a concentration of the

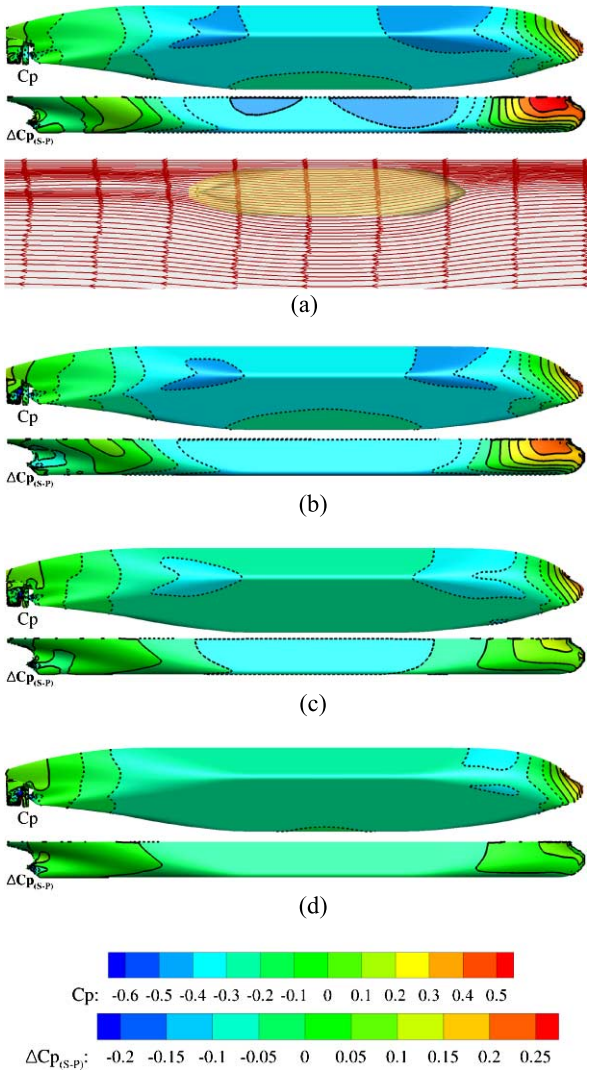

Fig. 19. Pressure distribution and difference against y_B ($h/T = 1.35$) in Canal A with *rotating* propeller. (a) C_P, $\Delta C_{P(S-P)}$ and streamlines at $y_B = 1.180$. (b) C_P and $\Delta C_{P(S-P)}$ at $y_B = 1.316$. (c) C_P and $\Delta C_{P(S-P)}$ at $y_B = 1.961$. (d) C_P and $\Delta C_{P(S-P)}$ at $y_B = 2.431$. (Colors are visible in the online version of the article; http://dx.doi.org/10.3233/ISP-130101.)

streamlines to starboard and the speed is high, giving rise to the pressure reduction in that region. Comparing the cases with non-rotating and rotating propeller, more suction force (Y') is generated on the hull with rotating propeller as greater low pressure area is produced on the parallel middle body, starboard side. As to the N' moment the pressure differences at the bow are almost unchanged, while with the

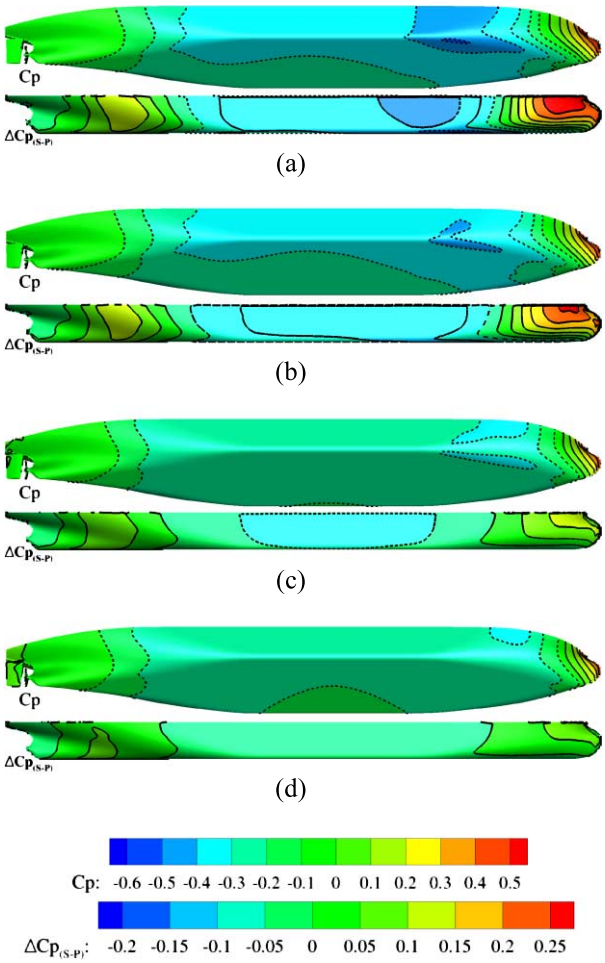

Fig. 20. Pressure distribution and difference against y_B ($h/T = 1.35$) in Canal B with *non-rotating* propeller. (a) C_P and $\Delta C_{P(S-P)}$ at $y_B = 0.758$. (b) C_P and $\Delta C_{P(S-P)}$ at $y_B = 0.909$. (c) C_P and $\Delta C_{P(S-P)}$ at $y_B = 1.632$. (d) C_P and $\Delta C_{P(S-P)}$ at $y_B = 2.173$. (Colors are visible in the online version of the article; http://dx.doi.org/10.3233/ISP-130101.)

rotating propeller the pressure is reduced at the stern, starboard side, contributing to a higher bow-out N' moment.

11. Streamlines on hull surface and horizontal planes

As shown above, the predicted pressure distribution offers a global view of the flow around the hull and an explanation of the forces and moments (particularly Y'

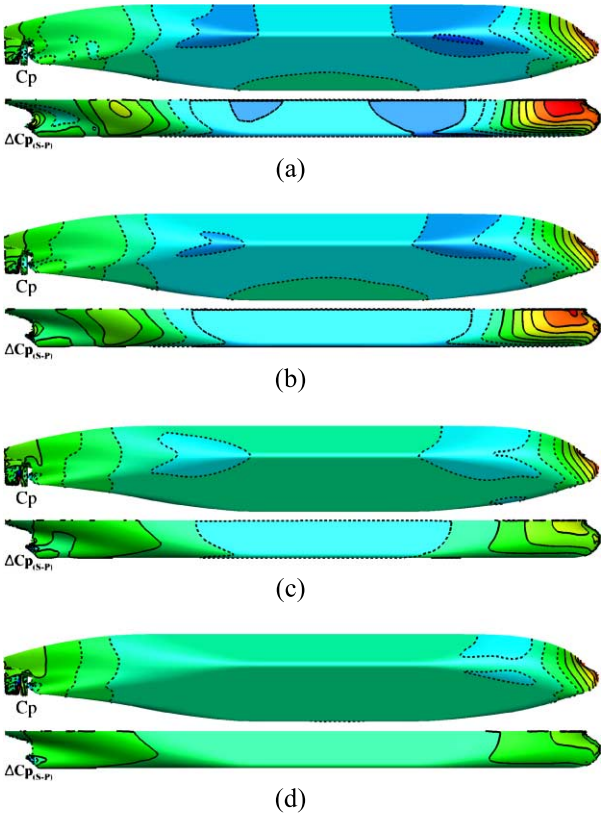

Fig. 21. Pressure distribution and difference against y_B ($h/T = 1.35$) in Canal B with *rotating* propeller. (a) C_P and $\Delta C_{P(S-P)}$ at $y_B = 0.758$. (b) C_P and $\Delta C_{P(S-P)}$ at $y_B = 0.909$. (c) C_P and $\Delta C_{P(S-P)}$ at $y_B = 1.632$. (d) C_P and $\Delta C_{P(S-P)}$ at $y_B = 2.173$. (Colors are visible in the online version of the article; http://dx.doi.org/10.3233/ISP-130101.)

and N') a ship encounters in a canal caused by the shallow-water and bank effects. In the present section, more details of the flow will be presented. The focus is on the aft-body where a massive flow separation occurs. Since this has a large influence on the X' force this will be discussed as well. To highlight the complexity of the flow in canals, a double model KVLCC2 hull in deep water (without any appendage) at the same Re number is considered for reference. As a benchmark case, it has been tested by many experimental institutes. For instance, the measured limiting streamlines in a wind tunnel were reported by Lee et al. [17].

The simulated limiting streamlines in unrestricted water, as well as the pressure distribution, are shown in Fig. 22, together with the streamlines on the water-plane. As can be seen, the limiting streamlines diverge around half draught but converge at the bilge indicating a strong bilge vortex. As for the divergence of the limiting

streamlines near the stern, at a saddle point S_1 the flow partly goes upwards towards the water-plane and partly almost vertically downwards to the propeller shaft where another saddle point S_2 is formed. A small bubble separation is found at the keel. The predicted limiting streamlines agree very well with the measurements by Lee et al. [17]. Negative pressures are noted at the aft-shoulder and bilge due to the large curvature of the hull surface; while towards the stern positive pressures are indicated.

In confined water the stern flow is much more complicated. Taking the extreme case with the shallowest water depth $h/T = 1.1$ and $y_B = 1.316$ in Canal A as an example, the predicted limiting streamlines on the solid walls (hull, rudder and propeller surfaces) together with the streamlines on the water-plane are exhibited in Fig. 23. The view is on the starboard side of the hull, as it faces the close side bank. Comparing with Fig. 22, the limiting streamlines are very different. Remarkable flow separations are noted, both of the bubble type and of the vortex sheet type. The bubble separation is characterized by a large recirculation area longitudinally starting at a saddle point S_{1c} near the bilge and extending upwards to the water-plane. Close to the waterline, a large vortex is developed leaving the hull surface. The saddle point S_{1c} seems to correspond to S_1 in the unrestricted water, see Fig. 22. In confined water it is moved much more upstream and downwards to the hull bottom. The flow around the stern is thus completely different with a massive separation. Thus, the flow moves in the upstream direction over the main part of the aft-body. Another bubble separation is noted near half draught, as demonstrated by the saddle point S_{3c}. This does not have any correspondence in the unrestricted case. It is located inside the large bubble separation. As will be seen below, the flow in the bubble behind S_{3c} originates from the port side of the hull, while the remaining flow inside the large bubble behind S_{1c} recirculates inside the main flow backwards on the starboard side. The strong vortex sheet separation is still noted close to the bilge, as indicated by the pronounced limiting streamlines convergence in that area. But it is located a bit more downwards than that in the unrestricted water case.

To better display the separation, "streamlines" on several horizontal planes are presented in Fig. 24, from top to bottom with an increasing distance from the water-plane. Positions of these horizontal planes on the hull are indicated in the figure as well. The "streamlines" are traced from the longitudinal and transverse velocity (U, V) vectors at each plane and are thus neither real streamlines nor projections of such streamlines on the plane. Nevertheless they can be used for illustrating recirculating flows and separations.

From the distribution of the "streamlines" over these planes, the asymmetric flow induced by the side bank and the massive separation region in the stern are noted. On the starboard side the separation starts just behind the aft-shoulder, and extends further and further backwards the deeper the plane. This means that the "outer" streamlines (outside the bubble) continue more or less straight backwards aft of the shoulder. They do not meet the streamlines from the port side immediately behind

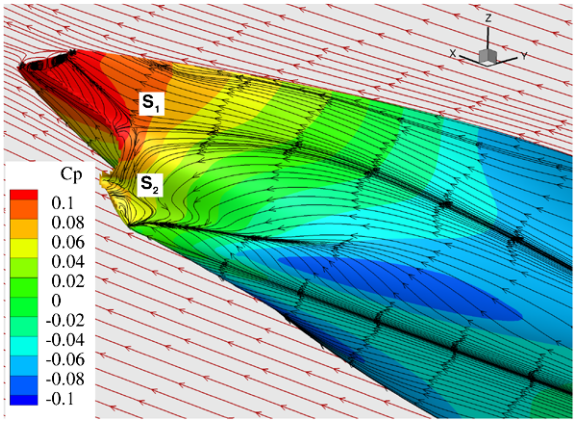

Fig. 22. Streamlines and pressure distributions on a double model KVLCC2 in unrestricted water. (Colors are visible in the online version of the article; http://dx.doi.org/10.3233/ISP-130101.)

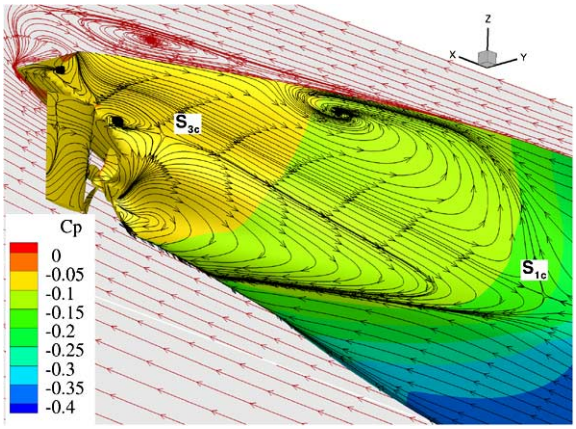

Fig. 23. Streamlines and pressure distributions at $h/T = 1.1$ and $y_B = 1.316$ in Canal A. (Colors are visible in the online version of the article; http://dx.doi.org/10.3233/ISP-130101.)

the stern, as they do in an unseparated flow. This means that the high pressure region normally found close to the stern and caused by the concave curvature of the streamlines in this region is absent. Comparing Figs 23 and 22 this effect is clearly seen.

Looking at the "streamlines" on the port side, they in fact exhibit a similar behavior. There is not much concave curvature near the stern. The curvature appears further aft, where the streamlines from the main flow on the two sides meet. Therefore the pressure is not very high even on the port side. (As will be seen below it is however slightly larger than on the starboard side.)

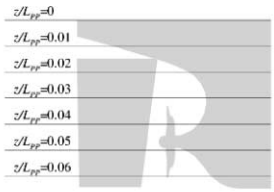

(a)

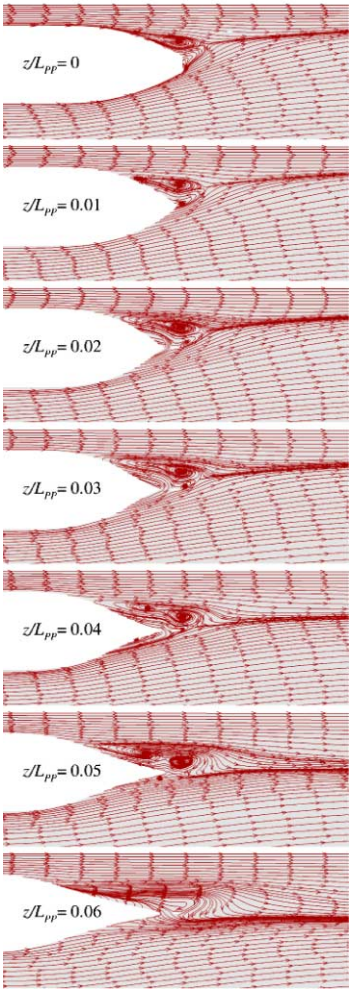

(b)

Fig. 24. Top view of "streamlines" on horizontal planes. (a) Positions of the horizontal planes. (b) From top to bottom: $z/L_{PP} = 0$, 0.01, 0.02, 0.03, 0.04, 0.05 and 0.06. (Colors are visible in the online version of the article; http://dx.doi.org/10.3233/ISP-130101.)

The missing high pressure region on the two sides of the stern causes a considerable increase in resistance. This is clearly seen in the plots of the X' force in Figs 12(a) and 13(a). For the present shallow water depth the resistance (solid line) is about three times that in unrestricted water (dash-dot line). The effect is reduced at the largest tested water depth where the ratio is about two. As seen in Fig. 25 the separation zone is reduced with the water depth, but it is still significant at $h/T = 1.5$.

Turning next to the influence on streamlines by different propeller performance, results of the closest ship-bank distance at $h/T = 1.35$ in Canal A with non-rotating and rotating propeller are presented in Figs 26 and 27, respectively. As shown in the limiting streamline figures, an operating propeller considerably changes the flow in front of it. In general, the propeller suction attracts the flow towards the propeller disc. There is however, a region of backward flow close to the surface even just in front of the propeller. The details will be explained in the next section.

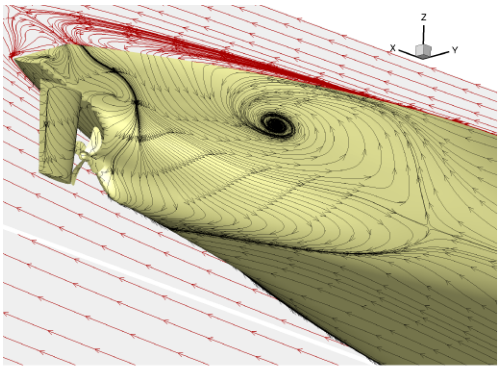

(a)

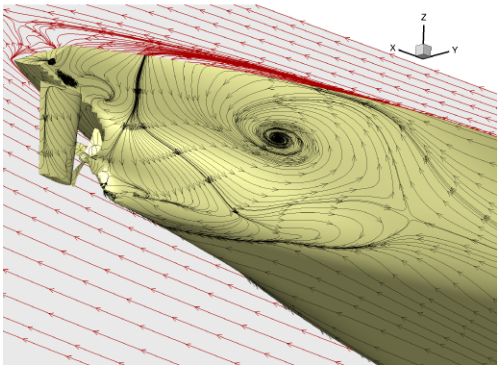

(b)

Fig. 25. Streamlines against water depth in Canal A. (a) $h/T = 1.35$. (b) $h/T = 1.5$. (Colors are visible in the online version of the article; http://dx.doi.org/10.3233/ISP-130101.)

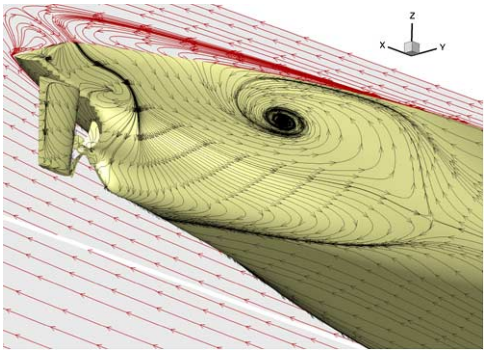

Fig. 26. Streamlines with *non-rotating* propeller: $h/T = 1.35$ and $y_B = 1.180$ in Canal A. (Colors are visible in the online version of the article; http://dx.doi.org/10.3233/ISP-130101.)

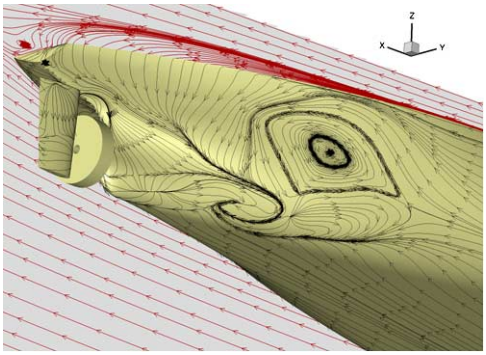

Fig. 27. Streamlines with *rotating* propeller: $h/T = 1.35$ and $y_B = 1.180$ in Canal A. (Colors are visible in the online version of the article; http://dx.doi.org/10.3233/ISP-130101.)

12. Hull-propeller-rudder interaction: Local pressure distributions, axial velocity contours and cross-flow vectors

In the present section more details of the flow without and with the rotating propeller will be presented for the cases seen in Figs 26 and 27. (The most extreme case with the rotating propeller.) Results are demonstrated by the local pressure distributions (C_P) on the port and starboard sides of the aft-body, together with the axial velocity contours ($U_{0\text{-rpm}}$ or U_{self}, seen from the stern) on the propeller plane $x/L_{PP} = -0.4825$ and the local cross-flow vectors around the propeller disc. Results with non-rotating and rotating propeller are shown in Figs 28 and 29, respectively.

With a non-rotating propeller, the pressure on the whole aft-body is small as explained above. Considering the large differences between the flows on the port and starboard side, revealed in Fig. 24, the pressures are surprisingly similar on the two sides. Far aft, the pressure is however slightly higher on the port side, which gives

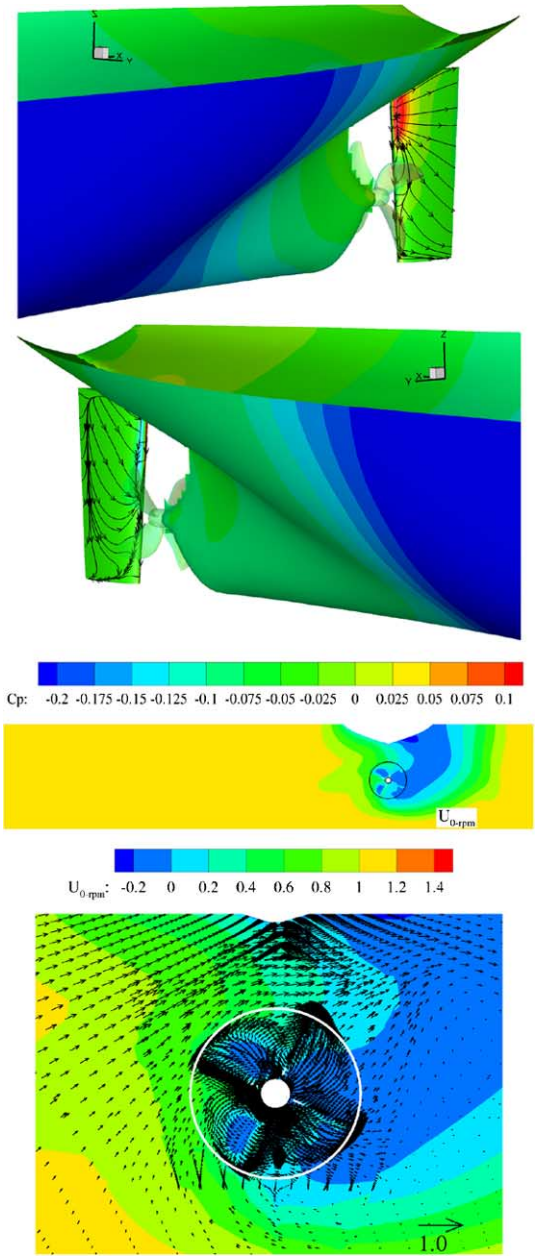

Fig. 28. Local pressure distributions on the surfaces and axial velocity contours/cross-flow vectors at the propeller plane: $h/T = 1.35$ and $y_B = 1.180$ in Canal A (*non-rotating* propeller). (Colors are visible in the online version of the article; http://dx.doi.org/10.3233/ISP-130101.)

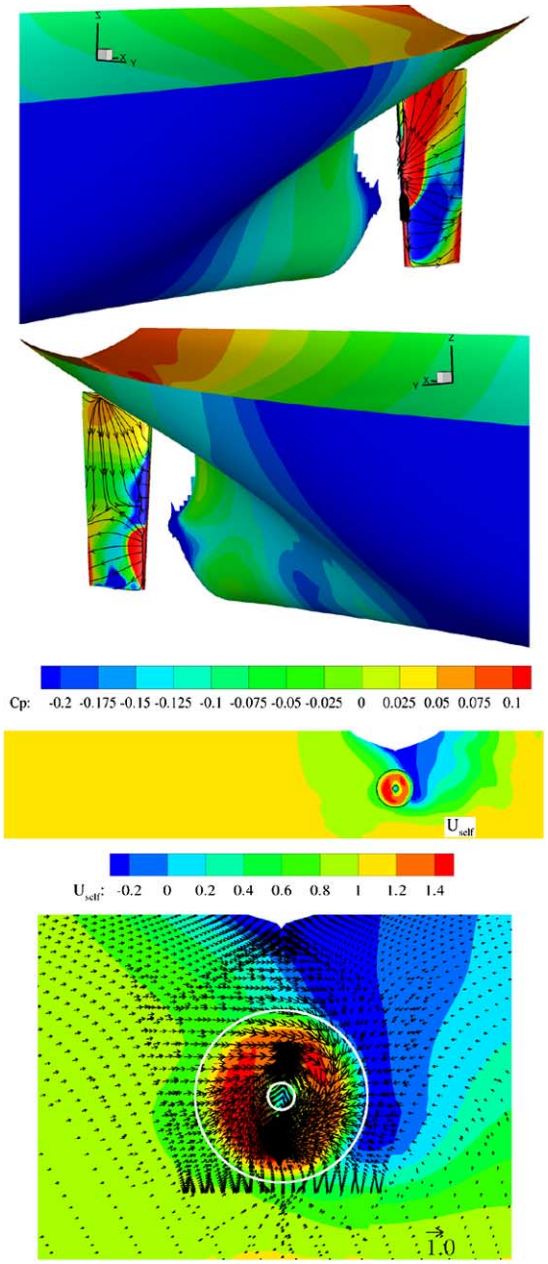

Fig. 29. Local pressure distributions on the surfaces and axial velocity contours/cross-flow vectors at the propeller plane: $h/T = 1.35$ and $y_B = 1.180$ in Canal A (*rotating* propeller). (Colors are visible in the online version of the article; http://dx.doi.org/10.3233/ISP-130101.)

rise to the negative pressure difference seen in this region in Fig. 18(a). In the upper part, near the leading edge of the rudder, a high pressure region appears on the port side and a low pressure region is on the opposite side. As mentioned above, there is a cross-flow from the port side into the separation bubble aft of S_{3c}. This is what causes the asymmetric pressure. The cross-flow is also clearly seen in the vector plot in Fig. 28, above the propeller disk. In fact there is a cross-flow in the other direction below the propeller disk, but its magnitude is much smaller and it has only a very small effect on the symmetry of the pressure.

To indicate the complex flow around the rudder the limiting streamlines there are displayed in the figure. On the port side the flow is essentially backwards, as can also be inferred from the "streamline" plots of Fig. 24. However, on the starboard side the rudder is within the recirculating region of the main separation bubble and the flow is essentially forwards. Obviously the rudder will not work well under such conditions.

When the propeller is rotating behind the hull, see Fig. 29, the pressure on the aft-body is decreased, as expected. The high pressure region above and behind the propeller is also as normally expected. Since the rudder operates in the slipstream, both the pressure and the streamlines have changed completely as compared to the case of Fig. 28. The stagnation in the upper part of the rudder in Fig. 28 has disappeared. Inside the propeller slipstream, the port side of the rudder has a high pressure area around the leading edge above the propeller shaft center-plane and a low pressure just below the center-plane. The opposite situation happens to the starboard side. This is a result of the right-handed rotation of the propeller slipstream, as illustrated by the axial velocity contours and the cross-flow vectors on the propeller plane.

Comparing the velocity contours of Figs 28 and 29 it is seen that the low speed region in the main separation bubble is reduced with the operating propeller, in accordance with the observations for the limiting streamlines. In unrestricted water the nominal wake is of course symmetric but the velocities have an upward component. This gives rise to an asymmetric loading, since the blades going down to starboard encounter a larger angle of attack than those going up to port. Therefore the starboard side of the propeller disk is more heavily loaded than the port one. Looking at the velocity contours in Fig. 29 it is seen that the velocities to port are larger than on the other side. This is opposite to what is expected for a right turning propeller, but is due to the fact that the velocities in the nominal wake are much smaller to starboard. The *increase* in velocity through the disk is larger on the starboard side. Since the velocity is so small in this region the propeller blades will have to operate at a very large angle of attack, like in bollard pull, and generate a large thrust. This is consistent with the larger reduction in pressure on the starboard side compared with the port side due to the propeller, and seen in Fig. 29. It is also consistent with the results of Fig. 14, where the propeller induces a bow-out moment.

Like in unrestricted water the reduced pressure around the stern creates an increased resistance force X' (thrust deduction). In Fig. 14 this is seen as the difference between the non-rotating and rotating cases. The magnitude of the effect seems to be as large as in unrestricted water.

13. Conclusions

Applying a steady state RANS method, confined-water effects on a KVLCC2 tanker appended with a rudder and a propeller in two canals have been studied in the present paper. The selected systematic conditions include both extremely shallow water depths and close ship-bank distances, which have made the computations rather difficult. In addition, propeller effects (at a zero propeller rate and at self-propulsion) have been taken into consideration. In earlier work, a grid convergence study and a formal validation study followed by an investigation of modeling errors were performed. Experiences from these preliminary studies provided knowledge of the numerical error/uncertainty, and most importantly, of the modeling errors in the RANS computations of this kind. In the present study the best available models were adopted. The predicted tendencies of viscous forces and moments in terms of varying water depth and ship-bank distance have shown to be qualitatively in accordance with the measurement data. The emphasis of the present paper is the predicted flow field, which is used to explain the effect of the confined water.

The predicted pressure distributions have offered an insight into the forces and moments acting on the hull. A high pressure region appears at the bow of the hull due to the stagnation. Further downstream the pressure is reduced more than in an unrestricted flow due to the blockage from shallow seabed and/or close side bank. The low pressure region starting from the fore-shoulder covers the whole parallel middle body on the starboard side, facing the bank, and is extended towards the stern region. However, the pressure gradually increases backwards due to the fact that the flow "escapes" to the port side under the bottom. At the stern the pressure is much lower than in an undisturbed flow due to a massive separation on the starboard side, starting near the aft shoulder. This separation causes a large recirculation zone extending backwards behind the rudder. The whole flow around the stern thereby gets asymmetric. In an unrestricted flow the streamlines from the two sides meet at the stern and create a high pressure. In the present case the streamlines outside the separation bubble meet further aft, so no high pressure is created at the stern. This causes a large increase in resistance, for the most extreme case about three times, as compared with the unrestricted water case.

The propeller increases the velocity around the aft-body, just like in unrestricted flow, but due to the very low velocities on the starboard side, this half of the propeller gets more heavily loaded. It therefore sucks more flow on the starboard side and the reduced pressure causes a bow-out moment on the hull with the rotating propeller.

Acknowledgements

The present work was funded by Chalmers University of Technology, Sweden and the China Scholarship Council. Computing resources were provided by C3SE, Chalmers Centre for Computational Science and Engineering. The authors thank

Mr. Guillaume Delefortrie (Flanders Hydraulics Research, Belgium) and Mr. Evert Lataire (Maritime Technology Division, Ghent University, Belgium) for providing the experimental data.

Appendix. Grid convergence study

The grid convergence study followed the method by Eça et al. [7], based on the Richardson Extrapolation (RE) and a Grid Convergence Index (GCI) proposed by Roache [26]. With Richardson Extrapolation, the grid discretization error δ_{RE} in a numerical solution can be expressed in a power series in the step size as:

$$\delta_{RE} = S_i - S_0 = \alpha h_i^p,$$

where S_i is the solution on the ith grid ($i = 1, 2, \ldots, n_g$, n_g – available number of grids $n_g > 3$); S_0 is the extrapolated solution to the zero step size; α is a constant; h_i represents the step size (grid spacing) of the ith grid and p is the order of accuracy in the numerical method.

To determine the three unknowns (S_0, α, p) in the equation above with more than three solutions, the observed order of accuracy p can be estimated through the curve fit of the Least Squares Root approach, minimizing the following function:

$$f(S_0, \alpha, p) = \sqrt{\sum_{i=1}^{ng} \left(S_i - \left(S_0 + \alpha h_i^p\right)\right)^2}.$$

The convergence condition is decided as below:

1. Monotonic convergence: $p > 0$.
2. Oscillatory convergence: $n_{ch} \geqslant \text{INT}(n_g/3)$, where n_{ch} is the number of triplets with $(S_{i+1} - S_i)(S_i - S_{i-1}) < 0$.
3. Anomalous behaviour: otherwise.

Three alternative error estimators are then introduced (the first two estimators are obtained from curve fit as well):

$$\delta_{RE}^{02} = S_i - S_0 = \alpha_{02} h_i^2,$$

$$\delta_{RE}^{12} = S_i - S_0 = \alpha_{11} h_i + \alpha_{12} h_i^2,$$

$$\delta_{\Delta_M} = \frac{\Delta_M}{(h_{n_g}/h_1) - 1},$$

where Δ_M is the data range, $\Delta_M = \max(|S_i - S_j|)$, $1 \leqslant i, j \leqslant n_g$, h_{ng} is the step size of the n_gth grid.

The numerical uncertainty still follows the form in [26]: $U_{SN} = F_S \cdot |\delta_{RE}|$, F_S is a factor of safety. Based on the convergence condition, the numerical uncertainty is formulated as follows:

1. Monotonic convergence:
   a. $0.95 \leqslant p \leqslant 2.05$: $U_{SN} = 1.25\delta_{RE} + U_{SD}$,
   b. $p \leqslant 0.95$: $U_{SN} = \min(1.25\delta_{RE} + U_{SD}, 3\delta_{RE}^{12} + U_{SD}^{12})$,
   c. $p \geqslant 2.05$: $U_{SN} = \max(1.25\delta_{RE} + U_{SD}, 3\delta_{RE}^{02} + U_{SD}^{02})$.
2. Oscillatory convergence: $U_{SN} = 3\delta_{\Delta M}$.
3. Anomalous behaviour: $U_{SN} = \min(3\delta_{\Delta_M}, 3\delta_{RE}^{12} + U_{SD}^{12})$, where U_{SD}, U_{SD}^{02}, U_{SD}^{12} are standard deviations of the curve fits.

References

[1] ASME V&V 20–2009, *Standard for Verification and Validation in Computational Fluid Dynamics and Heat Transfer*, American Society of Mechanical Engineers, New York, 2009.

[2] L. Broberg, B. Regnström and M. Östberg, SHIPFLOW theoretical manual, FLOWTECH International AB, Gothenburg, Sweden, 2007.

[3] P.W. Ch'ng, L.J. Doctors and M.R. Renilson, A method of calculating the ship-bank interaction forces and moments in restricted water, *International Shipbuilding Progress* **40**(421) (1993), 7–23.

[4] G. Delefortrie, K. Eloot and F. Mostaert, *SIMMAN 2012: Execution of model tests with KCS and KVLCC2. Version 2_0, WL Rapporten, 846_01*, Flanders Hydraulics Research, Antwerp, Belgium, 2011.

[5] G.B. Deng, P. Queutey and M. Visonneau, Three-dimensional flow computation with Reynolds stress and algebraic stress models, in: *Engineering Turbulence Modeling and Experiments*, Vol. 6, W. Rodi and M. Mulas, eds, Elsevier, 2005, pp. 389–398.

[6] E. Dick and J. Linden, A multi-grid method for steady incompressible Navier–Stokes equations based on flux difference splitting, *International Journal for Numerical Methods in Fluids* **14** (1992), 1311–1323.

[7] L. Eça, G. Vaz and M. Hoekstra, Code verification, solution verification and validation in RANS solvers, in: *Proceedings of ASME 29th International Conference OMAE2010*, June 6–11, 2010, Shanghai, China.

[8] L. Eça, G. Vaz and M. Hoekstra, A verification and validation exercise for the flow over a backward facing step, *V European Conference on Computational Fluid Dynamics, ECCOMAS CFD 2010*, J.C.F. Pereira and A. Sequeira, eds, June 2010, Lisbon.

[9] T.B. Gatski and C.G. Speziale, On explicit algebraic stress models for complex turbulent flows, *Journal of Fluid Mech.* **254** (1993), 59–78.

[10] T. Gourlay, Slender-body methods for predicting ship squat, *Ocean Engineering* **35**(2) (2008), 191–200.

[11] K.J. Han, Numerical optimization of hull/propeller/rudder configurations, Doctor thesis, Chalmers University of Technology, Gothenburg, Sweden, 2008.

[12] A. Hellsten and S. Laine, Extension of the k–ω-SST turbulence model for flows over rough surfaces, in: *AIAA-97-3577*, 1997, pp. 252–260.

[13] International Conference on Ship Maneuvering in Shallow and Confined Water: Bank Effects, Antwerp, Belgium, 2009, available at: http://www.bankeffects.ugent.be/index.html.

[14] L. Larsson and H. Raven (eds), *Ship Resistance and Flow*, Society of Naval Architects and Marine Engineers, New York, 2010.

[15] E. Lataire, M. Vantorre and K. Eloot, Systematic model tests on ship-bank interaction effects, in: *Proceedings of International Conference on Ship Maneuvering in Shallow and Confined Water: Bank Effects*, Antwerp, Belgium, May 2009.
[16] C.K. Lee and S.G. Lee, Investigation of ship maneuvering with hydrodynamic effects between ship and bank, *Journal of Mechanical Science and Technology* **22**(6) (2008), 1230–1236.
[17] S.J. Lee, H.R. Kim, W.J. Kim and S.H. Van, Wind tunnel tests on flow characteristics of the KRISO 3600 TEU containership and 300K VLCC double-deck ship models, *Journal of Ship Research* **47**(1) (2003), 24–38.
[18] D.Q. Li, Investigation on the propeller-rudder interaction by numerical methods, Doctor thesis, Chalmers University of Technology, Gothenburg, Sweden, 1994.
[19] D.Q. Li, M. Leer-Andersen, P. Ottosson and P. Trägårdh, Experimental investigation of bank effects under extreme conditions, in: *Practical Design of Ships and Other Floating Structures*, Elsevier Science, Oxford, 2001, pp. 541–546.
[20] D.C. Lo, D.T. Su and J.M. Chen, Application of computational fluid dynamics simulations to the analysis of bank effects in restricted waters, *Journal of Navigation* **62** (2009), 477–491.
[21] F.R. Menter, Zonal two equation k–ω turbulence models for aerodynamic flows, in: *24th Fluid Dynamics Conference*, Orlando, AIAA paper 93-2906, 1993.
[22] Q.M. Miao, J.Z. Xia, A.T. Chwang et al., Numerical study of bank effects on a ship travelling in a channel, in: *Proceedings of 8th International Conference on Numerical Ship Hydrodynamics*, Busan, Korea, 2003.
[23] J.N. Newman, The green function for potential flow in a rectangular channel, *Journal of Engineering Mathematics*, Anniversary Issue (1992), 51–59.
[24] N. Norrbin, Bank clearance and optimal section shape for ship canals, in: *26th PIANC International Navigation Congress*, Brussels, Belgium, Section 1, Subject 1, 1985, pp. 167–178.
[25] N. Norrbin, Bank effects on a ship moving through a short dredged channel, in: *10th ONR Symposium on Naval Hydrodynamics*, Cambridge, MA, 1974.
[26] P.J. Roache, Verification and validation in computational science and engineering, Hermosa Publishers, Albuquerque, 1998.
[27] P.L. Roe, Approximate Riemann solvers, parameter vectors, and difference schemes, *Journal of Computational Physics* **43** (1981), 357–372.
[28] E.O. Tuck, A systematic asymptotic expansion procedure for slender ships, *Journal of Ship Research* **8** (1964), 15–23.
[29] E.O. Tuck, Shallow water flows past slender bodies, *Journal of Fluid Mechanics* **26** (1966), 81–95.
[30] M. Vantorre, G. Delefortrie et al., Experimental investigation of ship-bank interaction forces, in: *Proceedings of International Conference on Marine Simulation and Ship Maneuverability, MARSIM'03*, Kanazawa, Japan, 2003.
[31] H.M. Wang, Z.J. Zou, Y.H. Xie and W.L. Kong, Numerical study of viscous hydrodynamic forces on a ship navigating near bank in shallow water, in: *Proceedings of the Twentieth International Offshore and Polar Engineering Conference*, June 20–25, 2010, Beijing, China.
[32] D.H. Zhang, Numerical computation of ship stern/propeller flow, Doctor thesis, Chalmers University of Technology, Gothenburg, Sweden, 1990.
[33] L. Zou, CFD predictions including verification and validation of hydrodynamic forces and moments on a ship in restricted waters, Licentiate thesis, Chalmers University of Technology, Gothenburg, Sweden, June 2011.
[34] L. Zou, L. Larsson, G. Delefortrie and E. Lataire, CFD prediction and validation of ship-bank interaction in a canal, in: *Proceedings of 2nd International Conference on Ship Maneuvering in Shallow and Confined Water*, Trondheim, Norway, 2011.
[35] L. Zou, L. Larsson and M. Orych, Verification and validation of CFD predictions for a maneuvering tanker, *Journal of Hydrodynamics, Ser. B* **22**(5) (2010), 438–445.